

Reduction of rain-induced errors for wind speed estimation on SAR observations using convolutional neural networks

Aurélien Colin^{1,2}, Pierre Tandeo^{1,3}, Charles Peureux², Romain Husson², Ronan Fablet^{1,3},

Abstract—Synthetic Aperture Radar is known to be able to provide high-resolution estimates of surface wind speed. These estimates usually rely on a Geophysical Model Function (GMF) that has difficulties accounting for non-wind processes such as rain events. Convolutional neural network, on the other hand, have the capacity to use contextual information and have demonstrated their ability to delimit rainfall areas. By carefully building a large dataset of SAR observations from the Copernicus Sentinel-1 mission, collocated with both GMF and atmospheric model wind speeds as well as rainfall estimates, we were able to train a wind speed estimator with reduced errors under rain. Collocations with in-situ wind speed measurements from buoys show a root mean square error that is reduced by 27% (resp. 45%) under rainfall estimated at more than 1 mm/h (resp. 3 mm/h). These results demonstrate the capacity of deep learning models to correct rain-related errors in SAR products.

Index Terms—Synthetic Aperture Radar, Deep Learning, Oceanography, Wind.

I. INTRODUCTION

SYNTHETIC Aperture Radar (SAR) is a powerful tool for studying the ocean surface. C-Band SAR are sensitive to variations in sea surface roughness, and have been used to detect various meteorological and ocean processes, referred to as metocean, such as atmospheric or ocean fronts [1], icebergs [2], oil surfactants from pollution [3] or generated by plankton [4], and some species of seaweed [5]. They are particularly useful for

studying waves [6] and extreme events like cyclones [7]. There has been particular attention given to estimating wind speed using these sensors.

As the number of satellite missions with C-SAR sensors increases and archives of these data accumulate, it is becoming easier to build large SAR datasets. This paper focuses on the Sentinel-1 mission from the Copernicus program, which consists of two satellites, Sentinel-1A (launched in 2014) and Sentinel-1B (launched in 2016, which has been out of operation since December 2021). Sentinel-1C is planned to be launched in 2023. Ground Range Detected Higher Resolution Interferometric Wide-swath (GRDH IW) observations have a range of 250 km, an azimuth of about 200 km, and a resolution of 10 m/px. These observations are mainly routinely acquired over coastal areas. Systematic processes are used to produce geophysical products from these observations, including wind speed estimates. Several Geophysical Model Functions (GMFs) have been developed for this purpose, including CMOD3 [8], CMOD4 [9], CMOD5 [10], CMOD5.N [11], CMOD6 [12], CMOD7 [13] and C_SARMOD2 [14]. However, these GMFs are sensitive to contamination from non-wind processes. In particular, rainfall can either increase or decrease sea surface roughness [15], making it difficult to correct for its effects.

Deep learning models, particularly Convolutional Neural Networks (CNNs), have demonstrated their ability to detect rain signatures in SAR observations [16]. These models are known to be able to tackle denoising [17] and inpainting [18] tasks because they use contextual information to estimate the

¹ IMT Atlantique, Lab-STICC, UMR CNRS 6285, F-29238, France.

² Collecte Localisation Satellites, Brest, France.

³ Odyssey, Inria/IMT, France

original signal. This paper is dedicated to estimating wind speed in rainy areas using a model that does not require an explicit rainfall prior and only uses the parameters available to GMFs.

In the first section, we present the SAR data used to train the model and the ancillary information available. The second section describes the methodology used to build the dataset, with special attention given to ensuring a balanced representation of rainfall observations. The final section presents the results on the training set and confirms them with in-situ measurements from buoys, demonstrating the model's ability to correct for rain overestimates/underestimates.

II. DATASET

The SAR measurements used in this chapter come from 19,978 IW observations acquired globally between March 03rd, 2018 and the February 23rd, 2022, inclusive. Each of these observations covers approximately 44 000 km² and has a resolution of 100 m/px, downsampled from the GRDH products available at 10 m/px.

Obtaining global information on rain that can be used in conjunction with SAR observations can be difficult. A previous study conducted using a global Sentinel-1 dataset found only 2,304 partial collocations with the satellite-based radar GPM-DPR [19] out of 18,2153 IW. "Partial collocations" refers to instances where at least 20x20 km of a swath is observed by the spaceborne weather radar 20 minutes before or after the SAR observation. Coastal ground-based radars like NEXRAD [20] could provide rainfall estimates, but they are affected by topography and may not capture all wind regimes. Therefore, SAR-based rain estimation is preferred to maximize the number of available observations and simplify the collocation process. We used a recent SAR rainfall estimator [16] that emulates NEXRAD's reflectivity and proposes three rainfall thresholds that roughly correspond to 1 mm/h, 3 mm/h, and 10 mm/h.

Ancillary information, such as incidence angle and satellite heading, is retrieved from Sentinel-1 Level-2 products. It also includes collocations with atmospheric models from the European Centre for

Medium-Range Weather Forecasts, which provide modelled wind speed and direction, as well as the surface wind speed computed by the GMF. The atmospheric models have a spatial resolution of 0.25x0.25 degrees and a temporal resolution of 3 hours, while the GMF has a spatial resolution of 1 km and corresponds to the observation itself."

III. METHODOLOGY

This section presents the methodology for building the rain-invariant wind speed estimator. We first describe the deep learning architecture of the model, then we discuss the creation of the dataset, which is biased to have a large number of rain examples. The final section describes the evaluation procedure.

A. Deep Learning Model

The architecture used in this chapter is the UNet architecture [21] depicted in Fig. 1. UNet is an autoencoder architecture with the advantage of being fully convolutional, meaning it has translation equivariance properties (translations of the input result in translations of the output). In addition, skip connections between the encoder and the decoder facilitate training, especially by reducing the vanishing gradient issue [22]). Introduced in 2015, UNet has been used in various domains and has demonstrated its importance for segmentation of SAR observations [23], [16], [24].

The output of the model always contains a single convolution kernel, activated by the ReLU function to ensure that the prediction is in the interval $[0, +\infty[$. All convolution kernels in the hidden layers are also activated by ReLU functions. The model is set to take input of 256x256 pixels during training, but since the weights only describe convolution kernels, it is possible to use the model for inference on images of any shape as long as the input resolution remains at 100 m/px. Variants of the model are trained with different numbers of input channels. The architecture is modified by changing the size of the first convolution kernel, which is defined as a kernel of size (3, 3, c, 32), where c is the number of input channels.

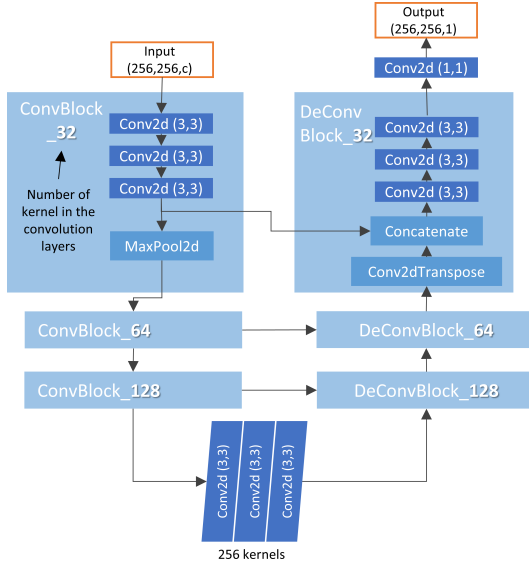


Fig. 1: Architecture of the UNet model used for estimating the wind speed.

B. Dataset balancing procedure

In this section, we describe the process for building a balanced dataset. Our goals are to (I) ensure that the wind distribution of each dataset is close to the real-world distribution, (II) prevent information leak between the training, validation, and test subsets, (III) ensure that the groundtruth wind speed, obtained from an atmospheric model, accurately represents the real-world wind speed, and (IV) include enough rain samples to allow the model to learn from them.

a) Rain and rainless patches selection: As discussed earlier, rainfall estimation is provided by a deep learning model at a resolution of 100 m/px, on the same grid as the SAR observation. Therefore, it is possible to separate the observations into two areas, \mathcal{A}^+ and \mathcal{A}^- , based on the 3 mm/h threshold from the rainfall estimation.

$$\mathcal{A}^+ = \{x : \text{Rainfall}(x) \geq 3 \text{ mm/h}\} \quad (\text{Eq. 1})$$

$$\mathcal{A}^- = \{x : \text{Rainfall}(x) < 3 \text{ mm/h}\} \quad (\text{Eq. 2})$$

However, most SAR observations do not contain rain signatures. Collocations with GPM's dual

polarization radar, a satellite-based weather radar, indicated that the probability of rain rates higher than 3 mm/h was 0.5%. Thus, by dividing the SAR observations into tiles of 256 by 256 pixels, we call "rain patches" the tiles with more than 5% of their surface predicted to have rain rates higher than 3 mm/h, and "rainless patches" those without rain signatures. We denote n_+ as the number of rain patches and n_- as the number of rainless patches. To ensure that the model will learn regardless of the rain-situation, we set $n_+ = n_-$.

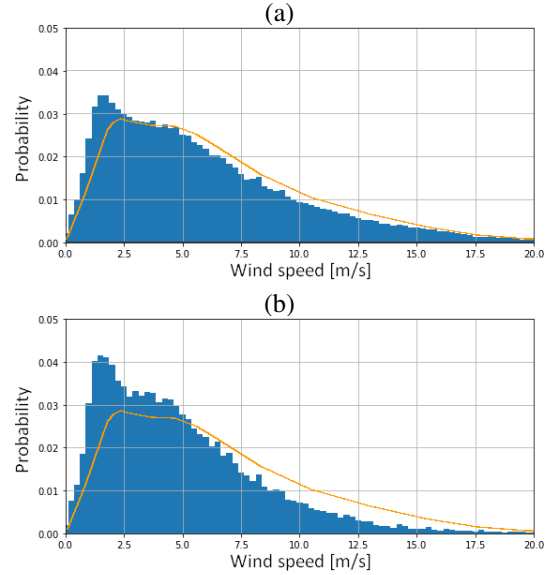


Fig. 2: Distribution of ECMWF ERA interim wind speed collocated with surface rain rate from GPM-DPR for rainfall higher than 3 mm/h (a) -0.55% of the collocations- and 30 mm/h(b) -0.02% of the collocations. The orange curve in the figure shows the wind distribution regardless of the rainfall.

b) Restriction to a priori Accurate Model Wind Speeds: Atmospheric models have been known to lack resolution (0.25x0.25 degrees spatially, 3 hours temporally) and to be unable to accurately depict fine-scale wind fields. However, they are computed globally and independently of the SAR observations. On the other hand, SAR-based wind fields from the GMFs are known to be accurate on rainless patches, but to overestimate on

rain signatures. We calculate Δ_{A-} as the discrepancy between the GMF and the atmospheric model on rain-free pixels.”

$$\Delta_{A-} = MSE_{|A-}(Atm, GMF) \quad (\text{Eq. 3})$$

In our experiments, the threshold was set at $\Delta_{A-} < 1$ m/s. All patches containing a higher discrepancy between the two wind speed sources were discarded.

c) Balancing to the real-world wind distribution: It should be noted that this condition ensures accurate modeled wind speeds and rain distribution, especially because the rainfall estimator is known to overestimate rainfall at high wind speeds.

We denote:

- P^+ as the wind speed distribution on n_+ .
- P^- as the wind speed distribution on n_- .
- P as the wind speed distribution on $n_- \cup n_+$.

Balancing the dataset to the real-world wind distribution translates to the following condition:

$$\forall x, P(x) = \frac{n_+ P^+(x) + n_- P^-(x)}{n_+ + n_-} \quad (\text{Eq. 4})$$

As we choose to keep all rain patches and to set $n_+ = n_-$, Eq. 4 leads to:

$$\forall x, P^-(x) = \frac{1}{2}(P^+(x) - P(x)) \quad (\text{Eq. 5})$$

For some wind speeds x , $P^+(x)$ is higher than twice $P(x)$. In these cases, we relax the condition from Eq. 5 in order to avoid removing rain patches. Fig. 3 depicts the wind speed distribution for rain and rainless patches. The mean squared error between P and $\frac{1}{2}(P^+ + P^-)$ reach 8.8%.

The dataset can be further balanced to ensure that, for each wind speed, the number of rain and rainless patches is equal. However, this leads to remove of 84% of the data. Appendix 1 compares the performance of this second dataset. As did not provide improvements, this dataset is left out of the main document.

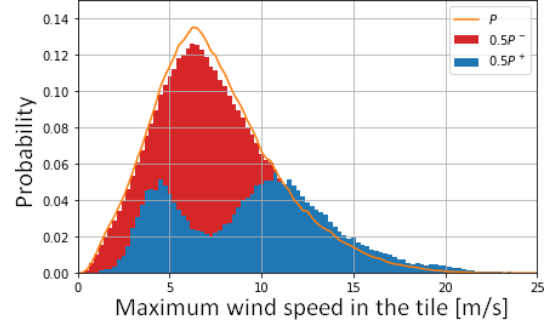


Fig. 3: Wind speed distributions for rain (blue) and rainless (red) patches. Orange curve correspond to the real world wind distribution.

1) Training, Validation and Test Set Division:

After extracting the patches following the distributions P^+ and P^- , they are split into training, validation, and test sets. Each subset preserves the same distributions. Furthermore, to avoid information leakage, if a patch from one IW is in a subset, every patch from the same IW belongs to the same subset. The stochastic brute forcing method described in Algorithm 1 draws random IWs and computes the distribution of the validation and test subsets, compares them to the overall distributions, and returns the solution that minimizes the difference. In this algorithm, \bar{P}_e indicates the wind speed distribution multiplied by the number of patches in e and divided by the total number of patches. It ensures that the validation and test subsets each contain approximately 10% of all the patches.

This process results in 168349, 20944, and 21010 patches in the train, test, and validation subsets, respectively, for 14169, 1763, and 1763 IWs.

Before training the model, we compute the mean and standard deviation of each channel on the training set and use them to normalize the inputs during training, validation, and inference. The output, however, is not normalized. We train the model for 100,000 weight updates, with a batch size of 16 and a learning rate of 10^{-5} using the Adam optimizer.

Algorithm 1: Stochastic brute forcing

input : The list L of all swath i and their patch distribution P_i .
output: L_{val} and L_{test} , the list of the swaths contained in the validation and test sets.

```

1  $\mathcal{L} = \text{MAE};$ 
2  $e_{min} = +\infty;$ 
3  $n_1 = \text{len}(L)/10;$ 
4  $n_2 = \text{len}(L)/3;$ 
5 for  $i \leftarrow 0$  to 1000000 by 1 do
6    $n = \text{random.integer}(\text{min}=n_1, \text{max}=n_2);$ 
7    $\text{candidate} = \text{random.choice}(L, \text{size}=n,$ 
    $\text{replace}=\text{False});$ 
8    $c_{val} = \text{candidate}[:n/2];$ 
9    $c_{test} = \text{candidate}[n/2:];$ 
10   $e_{val} = \mathcal{L}(0.1P^+, \bar{P}_{c_{val}}^-) + \mathcal{L}(0.1P^-, \bar{P}_{c_{val}}^-);$ 
11   $e_{test} =$ 
    $\mathcal{L}(0.1P^+, \bar{P}_{c_{test}}^+) + \mathcal{L}(P^-, 0.\bar{P}P_{c_{test}}^-);$ 
12   $e = \frac{2 \cdot e_{val} \cdot e_{test}}{e_{val} + e_{test}};$ 
13  if  $e < e_{min}$  then
14     $L_{val} = c_{val};$ 
15     $L_{test} = c_{test};$ 
16     $e_{min} = e;$ 
17  end
18 end

```

C. Evaluation procedure

To evaluate the impact of each input channel, we train various variants of the model:

- I uses only the VV channel.
- II uses the same inputs as the GMF: the VV channel, the incidence angle and the *a priori* wind speed direction.
- III uses the same inputs as II and the VH channel.
- IV uses the same inputs as III and the wind speed prior.
- V uses only the wind speed prior. We note that this variant implicitly use the VV channel, though at a resolution of only 1 km/px.

Each architecture is trained five times to reduce the impact of random initialization on the evaluation results. The results is presented as the mean and standard deviation over these five independent trainings.

We compare the results using the Root Mean Square Error (RMSE) and the Pearson correlation

coefficient (PCC). The PCC is formulated in Eq. 6.

$$PCC_{Y, \hat{Y}} = \frac{\mathbb{E}[(Y - \mu_Y)(\hat{Y} - \mu_{\hat{Y}})]}{\sigma_Y \sigma_{\hat{Y}}} \quad (\text{Eq. 6})$$

The results are computed against both the groundtruths from the atmospheric model, which provides a large test set, and against collocations with buoys, which have good temporal resolution and are in-situ measurements.

IV. RESULTS**A. Benchmarking experiments**

The performance of the models compared to ECMWF are calculated on the test subset for each input variant and the baseline GMF. The results of this analysis can be found in Table I. It appears that the most important input is the GMF itself, as both IV and V have better results than the other variants. I, II and III are unable to achieve better results than the GMF, except under strong rainfall, even though II and III have access to all the channels used by the GMF.

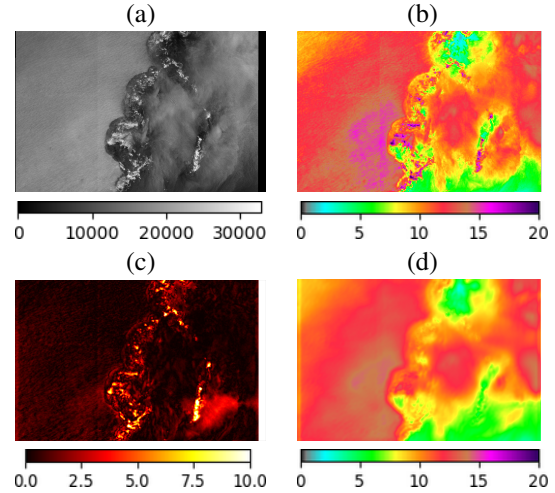


Fig. 4: Observation from the November 11th 2018 at 04:56:47. VV channel of the SAR observation (a), Geophysical model function estimated wind speed in m/s (b), deep learning estimated wind speed in m/s (d) and absolute difference between the two (c).

MODEL AND CHANNELS	RAIN RATE	RMSE		PCC	
		Balanced Dataset	Neutral Dataset	Balanced Dataset	Neutral Dataset
I [VV]	[0, 1[mm/h	1.38 [0.016]	2.40 [0.019]	89.9% [0.19%]	74.2% [0.42%]
	[1, 3[mm/h	1.64 [0.046]	2.78 [0.038]	92.7% [0.39%]	79.5% [0.58%]
	[3, 10[mm/h	1.59 [0.038]	3.18 [0.070]	92.7% [0.38%]	78.9% [0.62%]
	≥ 10 mm/h	2.12 [0.052]	★3.27 [0.135]	81.7% [1.03%]	74.3% [0.90%]
II [VV, INC, WDIR]	[0, 1[mm/h	0.87 [0.009]	2.26 [0.019]	96.2% [0.06%]	77.7% [0.24%]
	[1, 3[mm/h	1.04 [0.086]	2.87 [0.061]	97.2% [0.47%]	77.6% [0.24%]
	[3, 10[mm/h	1.19 [0.053]	3.39 [0.193]	96.2% [0.37%]	75.0% [3.04%]
	≥ 10 mm/h	2.27 [0.151]	3.86 [0.700]	81.7% [1.89%]	63.2% [9.19%]
III [VV, VH, INC, WDIR]	[0, 1[mm/h	0.83 [0.002]	2.18 [0.006]	96.5% [0.02%]	79.3% [0.07%]
	[1, 3[mm/h	0.93 [0.020]	2.73 [0.022]	97.7% [0.07%]	80.1% [0.29%]
	[3, 10[mm/h	1.09 [0.022]	3.25 [0.052]	96.7% [0.07%]	78.0% [0.44%]
	≥ 10 mm/h	2.13 [0.050]	3.68 [0.310]	83.9% [0.66%]	70.8% [2.95%]
IV [VV, VH, INC, WDIR, GMF]	[0, 1[mm/h	★0.64 [0.007]	★1.90 [0.028]	★97.9% [0.04%]	★85.0% [0.33%]
	[1, 3[mm/h	★0.63 [0.015]	★2.29 [0.075]	★98.9% [0.03%]	★87.1% [0.56%]
	[3, 10[mm/h	★0.78 [0.040]	★2.55 [0.132]	★98.4% [0.08%]	★87.1% [1.12%]
	≥ 10 mm/h	★1.63 [0.162]	3.37 [0.113]	★90.9% [1.17%]	73.4% [2.31%]
V [GMF]	[0, 1[mm/h	0.67 [0.003]	3.16 [2.650]	97.7% [0.02%]	80.7% [17.55%]
	[1, 3[mm/h	0.68 [0.005]	4.17 [3.582]	98.8% [0.01%]	82.5% [12.67%]
	[3, 10[mm/h	0.88 [0.021]	4.53 [3.739]	98.0% [0.03%]	83.4% [8.19%]
	≥ 10 mm/h	1.94 [0.087]	4.79 [2.917]	87.9% [0.66%]	74.0% [8.19%]
GMF	[0, 1[mm/h	0.77	2.41	97.0%	81.2%
	[1, 3[mm/h	0.84	3.16	98.1%	80.0%
	[3, 10[mm/h	1.25	3.42	96.5%	81.9%
	≥ 10 mm/h	4.65	3.70	52.5%	★ 75.4%

Table I: Comparison of the five variants of the model and the two datasets. RMSE and PCC are computed on the respective test set and for five training with random initialization. Results are given as mean and standard deviation in brackets. The best result for each metric is indicated by ★. Results better than the GMF are italicized.

B. Application to SAR observation with groundtruthed in-situ data

However, ECMWF wind speeds are reanalysis data and not in-situ data, which can be obtained using anemometers on buoys. Using the dataset created in [25], 4732 collocation points between Sentinel-1 and NDBC buoys are identified. The rain prediction model estimates that 4643 of these points are rainless, 75 record rainfall of more than 1 mm/h, and 14 record rainfall of more than 3 mm/h. On a side note, the height at which in-situ measurements were taken varies, with most being between 3.8 m and 4.1 m above sea level. As mentioned in [25], the SAR inversion and deep learning prediction are both normalized to the altitude of the corresponding in-situ measurement using an exponential law [26]:

$$w(h) = \left(\frac{10}{h}\right)^{0.11} \quad (\text{Eq. 7})$$

Table II indicates that the performances of the deep learning are higher than the GMF for both

the Root Mean Square Error and the Pearson Correlation Coefficient for all rain ranges. The RMSE decreases by 0.04, 0.39, and 1.33 m/s for rainless, light rain, and moderate rain-situations, respectively. The bias is also lower for the deep learning model, except for rainless situations.

Table II also demonstrates the importance of the dataset building scheme as a dataset composed of random collocations (without the aforementioned sample selection) between ECMWF and the GMF, referred to as the "neutral dataset," consistently has lower performances than the balanced dataset.

In the following, we observe two cases where rainfall was detected on the buoy position at the time of observation.

1) *2017-01-08 01:58:19 at NDBC 46054:* The observation from 2017-01-08 01:58:19 covers the north of the Californian Channel Islands (Fig. 5.a). Several meteorological buoys are dispersed over the channel, including NDBC 46054 and NDBC 46053, which are indicated as red dots. The wind speed

		Balanced Dataset	Neutral Dataset	GMF
Bias	< 1mm/h	0.73 [0.04]	1.32 [0.04]	★ 0.71
	[1, 3]mm/h	★ 1.38 [0.04]	1.47 [0.04]	1.64
	> 3mm/h	★ 0.92 [0.07]	1.96 [0.29]	2.93
RMSE	< 1mm/h	★ 1.44 [0.03]	1.76 [0.12]	1.48
	[1, 3]mm/h	★ 1.81 [0.04]	1.95 [0.18]	2.18
	> 3mm/h	★ 1.60 [0.10]	2.42 [0.21]	2.93
PCC	< 1mm/h	★ 93.6% [0.16%]	92.9% [0.20%]	93.4%
	[1, 3]mm/h	★ 96.3% [0.22%]	93.4% [0.19%]	95.3%
	> 3mm/h	★ 95.9% [0.35%]	93.4% [2.04%]	91.3%

Table II: Bias, Root Mean Square Error, and Pearson Correlation Coefficient of model IV, the GMF, for each rainfall level. The best result for each metric and rainfall level is indicated by ★. Results better than the baseline are in bold. Results are given as mean and standard deviation in brackets.

over the area is mostly around 6 m/s, but a squall line appears at the position of NDBC 46054 and spans over a dozen kilometers. Rain signatures are clearly visible on the southern (or upper, as the image is in sensor geometry) half of the front, which is detected by the rain detector. In the northern half, the backscattering is still high, but the rain signature is difficult to interpret. The GMF indicates very high wind speeds, higher than 20 m/s (Fig. 5.d), while the deep learning model attenuates these values to between 6 m/s and 8 m/s (Fig. 5.e). The southern half of the front, where rain signatures are visible, is the most attenuated.

For NDBC 46054, only one measurement of wind speed and direction per hour is available. It recorded a wind speed of 6.3 m/s eight minutes before the SAR observation. The GMF and the deep learning model estimated wind speeds of 15.1 m/s and 5.9 m/s, respectively. While the temporal resolution of NDBC 46054 is one measurement per hour, NDBC 46053 records data every ten minutes. Furthermore, the gust front appears to be moving toward the right part of the observation. This can be seen in the time series in Fig. 5 as a large variation in wind direction between 02:40:00 and 03:00:00. The variation in wind speed seems to precede the variation in direction, first increasing then decreasing to a lower wind regime. On NDBC 46053, the GMF and the deep learning model agree on a wind speed of 4.5 m/s, which is slightly lower than the in-situ data of 5.4 m/s. Since the distance between NDBC

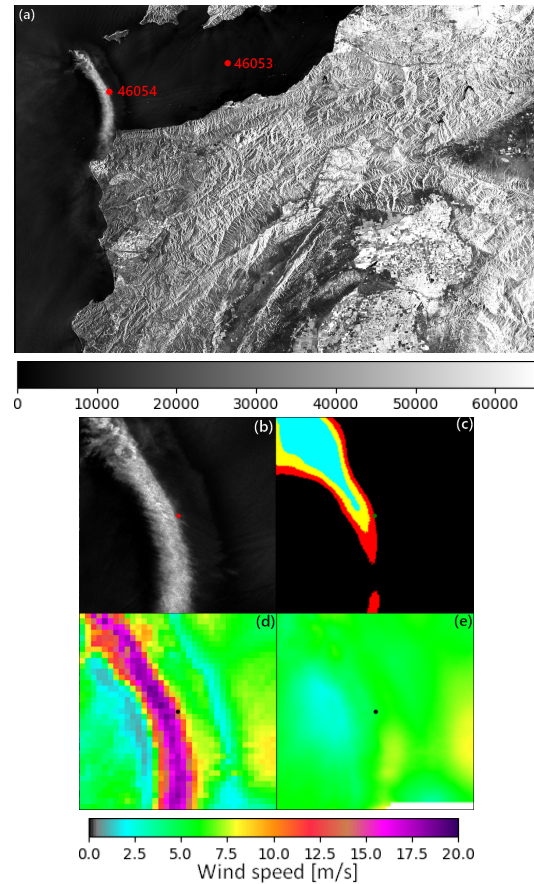


Fig. 5: Observation from the January 08th 2017 at 01:58:19 in VV channel (a), zoom on an area of 35x35 km centred on the buoy NDBC 45054 (b), segmentation of the rain rate (c), wind speed given by the GMF (d) and by the deep learning model (e).

46054 and NDBC 46053 is approximately 60 km, the progression of the gust front can be estimated to be around 90 km/h. With a width of around 5 or 6 km, the whole system would pass the buoys in three minutes. This means that even NDBC 46053 may not have been able to accurately estimate the wind speed due to its low temporal resolution. However, it is worth noting that even the gust speed at NDBC 46054, defined as the maximum wind speed over a given number of seconds, does not record a speed

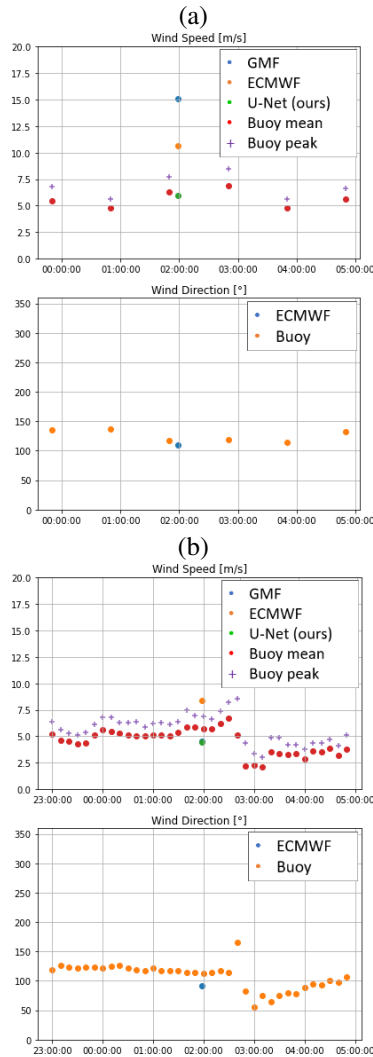


Fig. 6: Time series of the NDBC buoy wind measurements around January 08th 2017 01:58:19 for NDBC 46054 (a) and NDBC 46053 (b), and the estimation from the GMF, the deep learning model and the atmospheric model.

higher than 9 m/s.

2) SAR-20191006T232853 NDBC-41009:

The observation from 2019-10-06 23:28:53 was recorded on the east coast of Florida. While most of the swath covers the marshes around

Orlando and Cap Canaveral rather than the ocean, convective precipitation can be observed in the right part of the image (Fig. 7.a). The cells are moving downward (north-north-east), as indicated by the stronger gradient of the convective front. Since the wind from the convection is opposing the underlying wind regime, an area of lower wind speed appears as an area of lower backscatter. Rain signatures are clearly visible south of NDBC 41009 (Fig. 7.b). The GMF is impacted by these rain signatures and estimates a very high local wind speed (Fig. 7.c). The deep learning model is less affected by the rain signatures, but also appears to blur the low wind speed area (Fig. 7.d).

The time series from NDBC 41009 in Fig. 8 indicates that the lower backscattering was indeed caused by a drop in wind speed rather than a change in direction, as the latter does not significantly change during the passage of the convective cell (possibly because the underlying wind regime is strong). It does record a sudden drop in wind speed to 7.5 m/s one minute after the SAR observation, while the GMF and the deep learning model estimated wind speeds of 13.7 m/s and 8.9 m/s, respectively.

V. CONCLUSION

Previous studies have shown that high-resolution rain signatures can be automatically extracted from SAR observations. Using this SAR rainfall segmenter, we built a wind estimation dataset where 50% of the patches contain rainfall examples. Samples were chosen so that a SAR-based and a SAR-independent wind speed model agree on non-rain pixels, ensuring that their estimates are close to the true wind speed. A UNet architecture was trained on this dataset to estimate wind speeds based on the SAR-independent atmospheric model. We tested several input combinations and found that the most important parameter was the wind speed prior from the geophysical model function, which the deep learning model had difficulty emulating.

Collocations with buoy in-situ measurements show that the model outperforms the current Geophysical Model Function (GMF) on rain areas, reducing the RootMean Square Error (RMSE) by

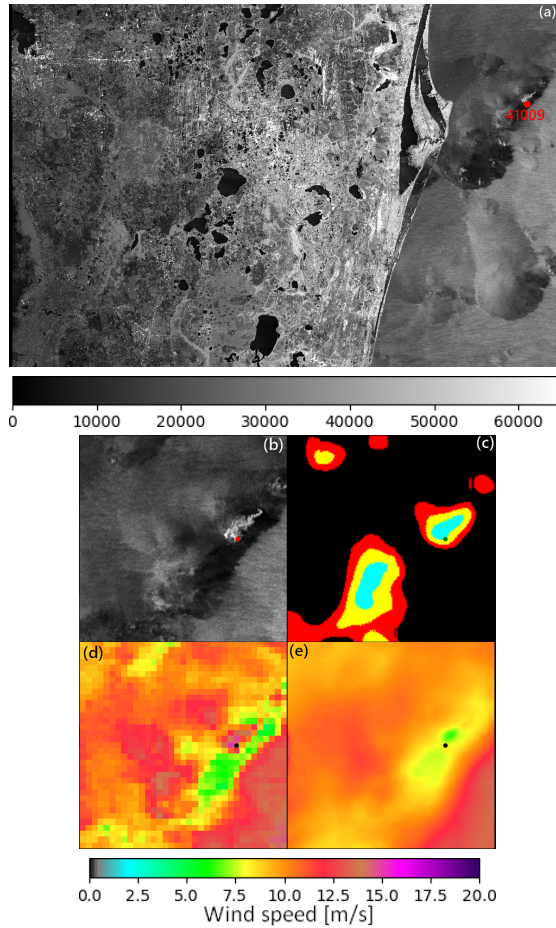


Fig. 7: Observation from October 06th 2019 at 23:28:53 in VV channel (a), zoom on an area of 35x35 km around the buoy NDBC 41009 (b), segmentation of the rain rate (c), wind speed given by the GMF (d) and by the deep learning model (e).

27% (resp. 45%) for rain rates higher than 1 mm/h (resp. 3 mm/h). On rainless areas, performances are similar with a small reduction of the RMSE by 2.7%. However, since the buoys have a time resolution of ten minutes, some quick sub-mesoscale processes, such as gust fronts, are difficult to register. The limited spatial range of the buoys also makes it challenging to observe rare phenomena.

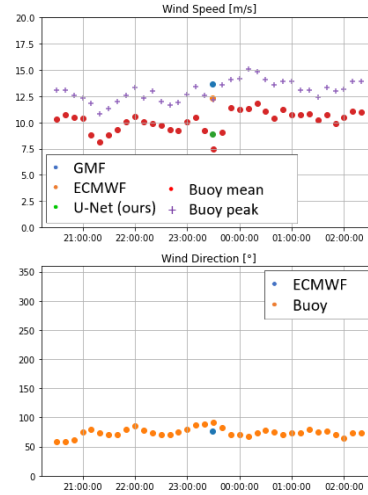


Fig. 8: Time series of the NDBC buoy wind measurements around October 06th 2019 at 23:28:53 for NDBC 41009, and the estimation from the GMF, the deep learning model and the atmospherical model.

Future work should address these concerns.

APPENDIX

A secondary dataset was created differing with the main dataset by Eq. 4. Here, the balancing policy is defined as:

$$\forall x, P(x) = P^+(x) = P^-(x) \quad (\text{Eq. 8})$$

The distributions P^+ and P^- are presented in Fig. 9. The balancing is performed for every wind speed, which lead to remove 84% of the rain patches -especially at 5 and 10 m/s- since the number of rain patches at 8 m/s is limited.

Comparison with the first balancing scheme display lower performances despite the more accurate balancing, as indicated Table III.

REFERENCES

- [1] C. Wang, P. Tandeo, A. Mouche, J. E. Stopa, V. Gressani, N. Longepe, D. Vandemark, R. C. Foster, and B. Chapron, "Classification of the global sentinel-1 SAR vignettes for ocean surface process studies," *Remote Sensing of Environment*, vol. 234, p. 111457, Dec. 2019. [Online]. Available: <https://doi.org/10.1016/j.rse.2019.111457>

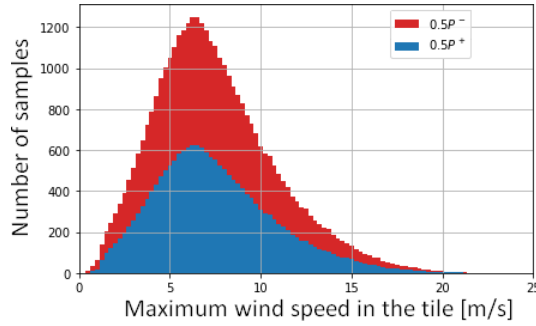


Fig. 9: Wind speed distribution for rain (blue) and rainless (red) patches.

	Dataset I	Dataset II	GMF
Bias	< 1mm/h	0.73 [0.04]	★ 0.71
	[1, 3]mm/h	★1.38 [0.04]	1.40 [0.10]
	> 3mm/h	0.92 [0.07]	★0.83 [0.14]
RMSE	< 1mm/h	★1.44 [0.03]	1.46 [0.06]
	[1, 3]mm/h	★1.81 [0.04]	1.85 [0.10]
	> 3mm/h	★1.60 [0.10]	1.61 [0.10]
PCC	< 1mm/h	★93.6% [0.16%]	93.3% [0.15%]
	[1, 3]mm/h	★96.3% [0.22%]	96.1% [0.23%]
	> 3mm/h	★95.9% [0.35%]	95.0% [0.46%]

Table III: Bias, Root Mean Square Error of model IV, the GMF, for each rainfall level. The best result for each rainfall level is indicated by ★. Results better than the baseline are in bold. Results of deep learning models are given as mean and standard deviation in brackets.

[2] M. M. Barbat, C. Wesche, A. V. Werhli, and M. M. Mata, “An adaptive machine learning approach to improve automatic iceberg detection from SAR images,” *ISPRS Journal of Photogrammetry and Remote Sensing*, vol. 156, pp. 247–259, Oct. 2019. [Online]. Available: <https://doi.org/10.1016/j.isprsjprs.2019.08.015>

[3] F. Ronci, C. Avolio, M. di Donna, M. Zavagli, V. Piccialli, and M. Costantini, “Oil spill detection from SAR images by deep learning,” in *IGARSS 2020 - 2020 IEEE International Geoscience and Remote Sensing Symposium*. IEEE, Sep. 2020. [Online]. Available: <https://doi.org/10.1109/igarss39084.2020.9323590>

[4] J. Svejksky and J. Shandley, “Detection of offshore plankton blooms with AVHRR and SAR imagery,” *International Journal of Remote Sensing*, vol. 22, no. 2-3, pp. 471–485, Jan. 2001. [Online]. Available: <https://doi.org/10.1080/014311601450040>

[5] H. Shen, W. Perrie, Q. Liu, and Y. He, “Detection of macroalgae blooms by complex SAR imagery,” *Marine Pollution Bulletin*, vol. 78, no. 1-2, pp. 190–195, Jan. 2014. [Online]. Available: <https://doi.org/10.1016/j.marpolbul.2013.10.044>

[6] F. Ardhuin, B. Chapron, and F. Collard, “Observation of

swell dissipation across oceans,” *Geophysical Research Letters*, vol. 36, no. 6, Mar. 2009. [Online]. Available: <https://doi.org/10.1029/2008gl037030>

[7] A. A. Mouche, B. Chapron, B. Zhang, and R. Husson, “Combined co- and cross-polarized SAR measurements under extreme wind conditions,” *IEEE Transactions on Geoscience and Remote Sensing*, vol. 55, no. 12, pp. 6746–6755, Dec. 2017. [Online]. Available: <https://doi.org/10.1109/tgrs.2017.2732508>

[8] A. Long, “C-band v-polarized radar sea-echo model from ERS-1 haltenbanken campaign,” *Journal of Electromagnetic Waves and Applications*, vol. 9, no. 3, pp. 373–391, Jan. 1995. [Online]. Available: <https://doi.org/10.1163/156939395x00532>

[9] A. Stoffelen and D. Anderson, “Scatterometer data interpretation: Estimation and validation of the transfer function CMOD4,” *Journal of Geophysical Research: Oceans*, vol. 102, no. C3, pp. 5767–5780, Mar. 1997. [Online]. Available: <https://doi.org/10.1029/96jc02860>

[10] H. Hersbach, “Cmod5 an improved geophysical model function for ers c-band scatterometry,” 2003. [Online]. Available: <https://www.ecmwf.int/node/9861>

[11] —, “Cmod5.n: A c-band geophysical model function for equivalent neutral wind,” 2008. [Online]. Available: <https://www.ecmwf.int/node/9873>

[12] A. Elyouncha, X. Neyt, A. Stoffelen, and J. Verspeek, “Assessment of the corrected CMOD6 GMF using scatterometer data,” in *SPIE Proceedings*, C. R. Bostater, S. P. Mertikas, and X. Neyt, Eds. SPIE, Oct. 2015. [Online]. Available: <https://doi.org/10.1117/12.2195727>

[13] A. Stoffelen, J. A. Verspeek, J. Vogelzang, and A. Verhoef, “The CMOD7 geophysical model function for ASCAT and ERS wind retrievals,” *IEEE Journal of Selected Topics in Applied Earth Observations and Remote Sensing*, vol. 10, no. 5, pp. 2123–2134, May 2017. [Online]. Available: <https://doi.org/10.1109/jstars.2017.2681806>

[14] Y. Lu, B. Zhang, W. Perrie, A. Mouche, X. Li, and H. Wang, “A c-band geophysical model function for determining coastal wind speed using synthetic aperture radar,” in *2018 Progress in Electromagnetics Research Symposium (PIERS-Toyama)*. IEEE, Aug. 2018. [Online]. Available: <https://doi.org/10.23919/piers.2018.8598163>

[15] W. Alpers, B. Zhang, A. Mouche, K. Zeng, and P. W. Chan, “Rain footprints on c-band synthetic aperture radar images of the ocean - revisited,” *Remote Sensing of Environment*, vol. 187, pp. 169–185, Dec. 2016. [Online]. Available: <https://doi.org/10.1016/j.rse.2016.10.015>

[16] A. Colin, P. Tandeo, C. Peureux, R. Husson, N. Longépé, and R. Fablet, “Rainfall estimation with sar using nexrad collocations with convolutional neural networks,” 2022. [Online]. Available: <https://arxiv.org/abs/2207.07333>

[17] G. Fracastoro, E. Magli, G. Poggi, G. Scarpa, D. Valsesia, and L. Verdoliva, “Deep learning methods for synthetic aperture radar image despeckling: An overview of trends and perspectives,” *IEEE Geoscience and Remote Sensing Magazine*, vol. 9, no. 2, pp. 29–51, Jun. 2021. [Online]. Available: <https://doi.org/10.1109/mgrs.2021.3070956>

[18] S. Wei, H. Zhang, X. Zeng, Z. Zhou, J. Shi, and X. Zhang, “CARNet: An effective method for SAR image interference suppression,” *International Journal of Applied Earth Observation and Geoinformation*,

vol. 114, p. 103019, Nov. 2022. [Online]. Available: <https://doi.org/10.1016/j.jag.2022.103019>

- [19] Precipitation Processing System (PPS) At NASA GSFC, “Gpm dpr precipitation profile 12a 1.5 hours 5 km v07,” 2021. [Online]. Available: <https://disc.gsfc.nasa.gov/datacollection/>
- [20] R. O. C. NOAA National Weather Service, “Noaa next generation radar (nexrad) level ii base data,” 1991. [Online]. Available: <https://www.ncei.noaa.gov/metadata/geoportal>
- [21] O. Ronneberger, P. Fischer, and T. Brox, “U-net: Convolutional networks for biomedical image segmentation,” *CoRR*, vol. abs/1505.04597, 2015. [Online]. Available: <http://arxiv.org/abs/1505.04597>
- [22] R. Pascanu, T. Mikolov, and Y. Bengio, “On the difficulty of training recurrent neural networks,” 2012. [Online]. Available: <https://arxiv.org/abs/1211.5063>
- [23] A. Colin, R. Fablet, P. Tandeo, R. Husson, C. Peureux, N. Longépé, and A. Mouche, “Semantic segmentation of metoceanic processes using SAR observations and deep learning,” *Remote Sensing*, vol. 14, no. 4, p. 851, feb 2022. [Online]. Available: <https://doi.org/10.3390/rs14040851>
- [24] I. de Gelis, A. Colin, and N. Longepe, “Prediction of categorized sea ice concentration from sentinel-1 SAR images based on a fully convolutional network,” *IEEE Journal of Selected Topics in Applied Earth Observations and Remote Sensing*, vol. 14, pp. 5831–5841, 2021. [Online]. Available: <https://doi.org/10.1109/jstars.2021.3074068>
- [25] L. de Montera, H. Berger, R. Husson, P. Appelghem, L. Guerlou, and M. Frago, “High-resolution offshore wind resource assessment at turbine hub height with sentinel-1 synthetic aperture radar (SAR) data and machine learning,” *Wind Energy Science*, vol. 7, no. 4, pp. 1441–1453, Jul. 2022. [Online]. Available: <https://doi.org/10.5194/wes-7-1441-2022>
- [26] E. W. Peterson and J. P. Hennessey, “On the use of power laws for estimates of wind power potential,” *Journal of Applied Meteorology*, vol. 17, no. 3, pp. 390–394, Mar. 1978. [Online]. Available: [https://doi.org/10.1175/1520-0450\(1978\)017<0390:otupl>2.0.co;2](https://doi.org/10.1175/1520-0450(1978)017<0390:otupl>2.0.co;2)



Aurélien COLIN After graduating from the IMT Atlantique as an engineer, he began a Ph.D and is currently studying the segmentation of various meteorological and ocean phenomena on Synthetic Aperture Radar using deep learning models.



Pierre TANDEO was born in France in 1983. He received the M.S. degree in applied statistics from Agrocampus Ouest, Rennes, France, and the Ph.D. degree from the Oceanography from Space Laboratory at IFREMER, Brest, France, in 2010. Then, he spent two years as a Postdoctoral Researcher with the Atmospheric Science Research Group, University of Corrientes, Argentina, and three years at Télécom Bretagne, Brest, France. Since 2015, he is an associate professor at IMT Atlantique, Brest, France, and a researcher at Lab-STICC, CNRS, France. Since 2019, he is an associate researcher at the Data Assimilation Research Team, RIKEN Center for Computational Science, Kobe, Japan. His main research interests are focused on IA, data assimilation, and inverse problems for geophysics.



Charles PEUREUX is a research engineer at CLS since 2020 where he is mainly involved with SAR oceanography. He previously worked at IFREMER where he defended his thesis on the observation and modelling of the directional properties of short gravity waves. Thereafter, he worked on the SKIM satellite mission, especially for the production of high resolution sea state numerical simulations.



Romain HUSSON is a scientist and project engineer at CLS, in the Environmental Monitoring and Climate Business Unit. After working as intern at NASA JPL and as YGT at ESRIN on SAR wind-wave-current activities, he completed in 2012 his PhD in Physical Oceanography at CLS Brest developing methods to estimate synthetic swell field from SAR wave mode observations. Since then, he has been involved in several applicative and R&D projects such as wind/wave products for marine renewable energy and contributed to several ESA and European projects such as Cal/Val activities for ENVISAT and S-1 mission performance center as Level-2 expert.



Ronan FABLET is a Professor at IMT Atlantique and a research scientist at Lab-STICC in the field of Data Science and Computational Imaging. He is quite involved in interdisciplinary research at the interface between data science and ocean science, especially space oceanography and marine ecology. His current research interests include deep learning for dynamical systems and applications to the understanding, analysis, simulation and reconstruction of ocean dynamics, especially using satellite ocean remote sensing data.